npj | flexible electronics

Article

Published in partnership with Nanjing Tech University

https://doi.org/10.1038/s41528-025-00493-6

Fully stretchable hydrovoltaic cells based on winding-locked double-helical carbon nanotube fibers

Wonkyeong Son[1,7], Jae Myeong Lee[1,7], Hyunji Seo[1], Gyu Hyeon Song[1], Seon Jeong Kim[1], Sooncheol Kwon[2], Sung Beom Cho[3], Sungwoo Chun[4], Shi Hyeong Kim[5,6] ✉ & Changsoon Choi[1] ✉

Hydrovoltaic power generators that convert water–nanomaterial interactions into electricity represent a promising route for sustainable energy harvesting. However, most previous studies have relied on non-stretchable planar designs, requiring continuous water flow or ionic solutions. Here, we present a fully stretchable hydrovoltaic cell (FSHC) with a parallel double-helix configuration of neat and oxidized carbon nanotube (CNT) fibers wound around an elastomeric core. This winding-locked double-helix architecture ensures mechanical robustness and stable electrical properties under strain. When immersed in quiescent deionized water, the FSHC generates ~0.31 V and ~22.4 μA/cm^2, maintaining reliable performance up to 200% strain. To demonstrate its potential in wearable applications, the FSHC is integrated into a fabric glove. Moreover, multiple FSHCs connected in series or parallel provide sufficient power to drive a twisted CNT fiber actuator. This study introduces a deformable hydrovoltaic platform for fiber-based energy harvesters, broadening their applicability to wearable electronics and self-powered actuation.

Water, which covers about 71% of the Earth's surface area, contains considerable energy in various forms that dominate energy transfer in many natural phenomena[1,2]. Converting the mechanical and chemical energy of water into electricity has become increasingly important for sustainable and eco-friendly power generation[3–5]. Hydrovoltaic technologies[6,7], which leverage the interfacial interactions between water and nanostructured materials, have emerged as a promising approach for harvesting energy from various forms of water such as flows[8–10], waves[11–13], droplets[14–19], and moisture[20–24]. To date, a variety of strategies based on different mechanisms, including electrokinetic effects, alternating potentials, and ionic diffusion, have been explored. For instance, in 2014, Guo et al. discovered that a single water droplet interacting with graphene could generate electricity, thus revealing the electrokinetic potential at the liquid–solid interface[15]. In 2015, Qu et al. showed that a graphene oxide framework sandwiched between two grid-patterned gold electrodes could produce intermittent electrical signals through moisture diffusion[20]. In 2017, Guo et al. demonstrated that natural water evaporation could be exploited using a porous nanostructured graphite film to achieve continuous power generation[25]. More recently, in 2023, Li et al. advanced droplet-based hydrovoltaics, achieving potentials above 1200 V by optimizing electric double-layer dynamics at interfaces[26]. Building upon these advancements, Yuan et al. in 2024 developed a hermetic hydrovoltaic cell with internal water circulation driven by temperature fluctuations, enabling stable long-term electricity generation without water loss[27].

Despite the significant progress achieved in these pioneering studies, current hydrovoltaic devices still face two critical challenges that hinder their practical potential and applicability. First, their electrical output inherently depends on either continuous charge carrier movement or steady ionic concentration gradients, meaning that any interruption or equilibrium in these conditions rapidly terminates electricity generation. Second, most previously reported hydrovoltaic devices are typically composed of rigid or non-stretchable substrates and functional materials, limiting their adaptability to dynamic and mechanically active environments. Although stretchability has rarely been implemented in hydrovoltaic systems, substantial advances have been achieved in other types of energy harvesters based on photovoltaic, thermoelectric, and triboelectric effects[28–30]. These devices have demonstrated stable energy generation under large tensile strains, enabling integration into wearable and deformable platforms. To

[1]Department of Electronic Engineering and Biomedical Engineering, Hanyang University, Seoul, Republic of Korea. [2]Department of Energy and Materials Engineering, Dongguk University-Seoul, Seoul, Republic of Korea. [3]Department of Materials Science and Engineering, Ajou University, Suwon, Republic of Korea. [4]Department of Electronics and Information Engineering, Korea University, Sejong, Republic of Korea. [5]Textile Innovation R&D Department, Korea Institute of Industrial Technology, Ansan, Gyeonggi-do, Republic of Korea. [6]Department of Advanced Material Engineering, Chung-Ang University, Anseong, Gyeonggi-do, Republic of Korea. [7]These authors contributed equally: Wonkyeong Son, Jae Myeong Lee. ✉e-mail: shk@kitech.re.kr; pccs2004@hanyang.ac.kr

achieve this combination of stable electrical performance and mechanical flexibility, two main strategies have been widely adopted: (i) using intrinsically elastic functional materials (*e.g.*, elastomers, hydrogels) and (ii) designing structurally stretchable architectures (*e.g.*, helices, buckles, and kirigami structures). In this context, developing hydrovoltaic devices capable of reliably generating electricity from the environment with few constraints and maintaining stable performance under mechanical deformation remains an urgent challenge for practical applications. To address these limitations, a yarn-based flexible carbon–water device that converts chemical energy in the nanotube yarn into electricity has been reported, enabling water-based power generation without requiring flowing water or ionic solutions[31]. Such demonstrations have opened up new possibilities for designing advanced hydrovoltaic devices with exceptional flexibility and adaptability, thereby supporting their integration into practical and versatile systems.

In this work, we propose a fully stretchable hydrovoltaic cell (FSHC) with a winding-locked double-helix design, in which two carbon nanotube (CNT) fibers (neat and oxidized) electrochemically interact with water molecules. Specifically, the wettability difference between the hydrophobic neat CNT (NCNT) fiber and the hydrophilic oxidized CNT (OCNT) fiber induces asymmetric charge interactions at the CNT–water interfaces, establishing a potential difference. To achieve structural stretchability, these CNT fiber electrodes are helically wound around an elastomeric core prestrained to 200% of its original length, thereby maintaining a constant gap between them. Upon release of the prestrain, the elastomer—which had been stretched and thinned—returns to its original dimensions *via* radial recovery governed by Poisson's ratio. During this relaxation, the double-helix structure becomes self-locked, forming an intimate contact interface between the CNT fibers and the core. This simple and reliable assembly process eliminates the need for an additional separator. The resulting winding-locked architecture not only offers high structural integrity but also ensures exceptional durability under mechanical deformations. When in contact with quiescent deionized water, the FSHC produces a high electrical output with an open-circuit voltage of ~0.31 V and a short-circuit current of ~22.4 μA/cm^2. More importantly, owing to the rational double-helix design and winding-lock effect, the FSHC shows remarkable mechanical robustness, withstanding repeated stretching up to 200% strain without notable degradation in electrical performance. To the best of our knowledge, such a high degree of stretchability has not been previously reported in fiber- or yarn-based hydrovoltaic devices, validating the unique advantages of our winding-locked architecture. To further demonstrate its practical applicability, the FSHC fibers are sewn into a glove, confirming their feasibility for integration into textile-based wearable systems. Moreover, by connecting multiple FSHCs in series or parallel as an energy-harvesting module, the enhanced power output is sufficient to directly drive fiber-type electrochemical torsional actuators consisting of twisted CNT fibers in an electrolyte. This study presents an effective strategy for fabricating stretchable hydrovoltaic devices suitable for wearable electronics, greatly broadening their potential applications in self-powered actuation systems.

Results

Fabrication and morphological information of the FSHC

Figure 1a and Supplementary Fig. 1 illustrate the stepwise fabrication of the FSHC, which involves three key steps: (i) prestrain application, (ii) electrode winding, and (iii) strain relaxation. To construct the stretchable hydrovoltaic architecture, a commercially available silicone elastomer was molded into a cylindrical shape using a needle-tip template, as detailed in the Experimental section. This elastomeric core served as the flexible substrate, providing mechanical compliance and elasticity under repeated deformations. In the first step, the as-fabricated elastomeric core (length: 20 mm, diameter: 0.6 mm) was stretched uniaxially to 200% of its original length. This prestrain application was critical for achieving tight integration of the CNT fiber electrodes with the elastomeric core after strain relaxation. By maintaining the elastomer in a highly elongated state, the subsequent CNT fiber winding process ensured that the fibers were securely positioned around the core without unintended displacement or detachment. In the second step, two CNT fibers were tightly wound around the elastomeric core in a parallel configuration. These fibers were prepared by twisting sheets of aligned multiwalled CNTs drawn from forests[32]. Ethanol was repeatedly applied to the elastomer surface to densify the fibers during evaporation[33–35]. In the third step, strain relaxation was induced by releasing the prestrain in the elastomeric core, allowing it to contract back to its original dimensions. This contraction, governed by Poisson's effect, generated a radial expansion that effectively secured the CNT fibers onto the elastomeric core to form a self-locking structure. Due to ethanol densification, the adhesion between the CNT fibers and elastomer core remained strong, and no noticeable detachment was observed during tensile strain relaxation. As a result, the CNT fibers became firmly anchored to the elastomeric core without the need for additional adhesives. This winding-locked configuration not only enhanced the mechanical robustness of the FSHC but also ensured a stable electrode-substrate interface, preventing fiber slippage or delamination under mechanical deformation. When the FSHC was exposed to water (inset, Fig. 1a), a potential difference developed between the two CNT fiber electrodes, leading to electricity generation. This phenomenon originated from the distinct surface properties of the NCNT and OCNT fibers, which caused asymmetric interactions with water molecules. Specifically, the NCNT fiber remained hydrophobic and repelled water, thereby minimizing direct charge transfer at the solid–liquid interface. In contrast, the OCNT fiber exhibited strong hydrophilicity due to the presence of oxygen-containing functional groups, thereby allowing enhanced water adsorption. This asymmetric wettability between the two electrodes induced different charge-transfer interactions, facilitating hydrovoltaic energy conversion[31].

First, these differences were elucidated by the SEM images (Supplementary Fig. 2). The NCNT fiber showed a smooth and compact structure (Supplementary Fig. 2a, c), whereas the OCNT fiber displayed a rougher and more disordered morphology (Supplementary Fig. 2b, d). This structural difference resulted from the presence of oxygen-containing functional groups, which disrupt the graphitic stacking of the CNT bundles. Moreover, the successful oxidation of the CNT fiber to obtain the OCNT was confirmed by X-ray photoelectron spectroscopy (XPS) results (Supplementary Fig. 3). Specifically, the O/C ratio of the OCNT increased to 0.27, compared to 0.11 for the NCNT, indicating a significant incorporation of oxygen-containing functional groups. This chemical modification altered the surface charge distribution of the OCNT, which enhanced its ability to interact with water molecules and facilitated charge transfer at the electrode–water interface. The intensity ratio between the D and G bands (I_D/I_G) from the Raman spectra (Supplementary Fig. 4)—which represents the degree of atomic defects in the CNT structure—increased from 0.52 for the NCNT to 0.82 for the OCNT, supporting the XPS results described above. In addition, the mechanical properties of the NCNT and OCNT fibers were examined using the stress-strain curves (Supplementary Fig. 5). The tensile strength of the OCNT fibers decreased by 25.8% (109.5 MPa) compared to that of the NCNT fibers (147.5 MPa). This reduction was attributed to the partial disruption of sp^2-hybridized bonds in the CNT network caused by oxidation-induced defects. Nevertheless, the introduction of oxygen functionalities facilitated the formation of intermolecular hydrogen bonds, leading to a slight increase in the maximum strain from 5.1% to 5.5%[36,37].

The parallel double-helix configuration of the CNT fiber electrodes in the FSHC was revealed by the optical micrographs (Fig. 1b). This uniform helical arrangement ensured a well-defined electrode alignment, preserving both structural stability and mechanical flexibility. The precisely controlled fiber winding process minimized irregularities that could otherwise compromise the device performance. A magnified view of the electrode arrangement is shown in Fig. 1c, indicating the presence of a well-defined and consistent interstitial spacing between the helical CNT fibers. This spacing was essential for preventing electrical shorting while simultaneously facilitating efficient charge separation, both of which are crucial for stable hydrovoltaic energy conversion. The uniformity of this spacing also suggested a high degree of reproducibility in the fabrication process. The intimate contact between the CNT fibers and elastomeric core after prestrain

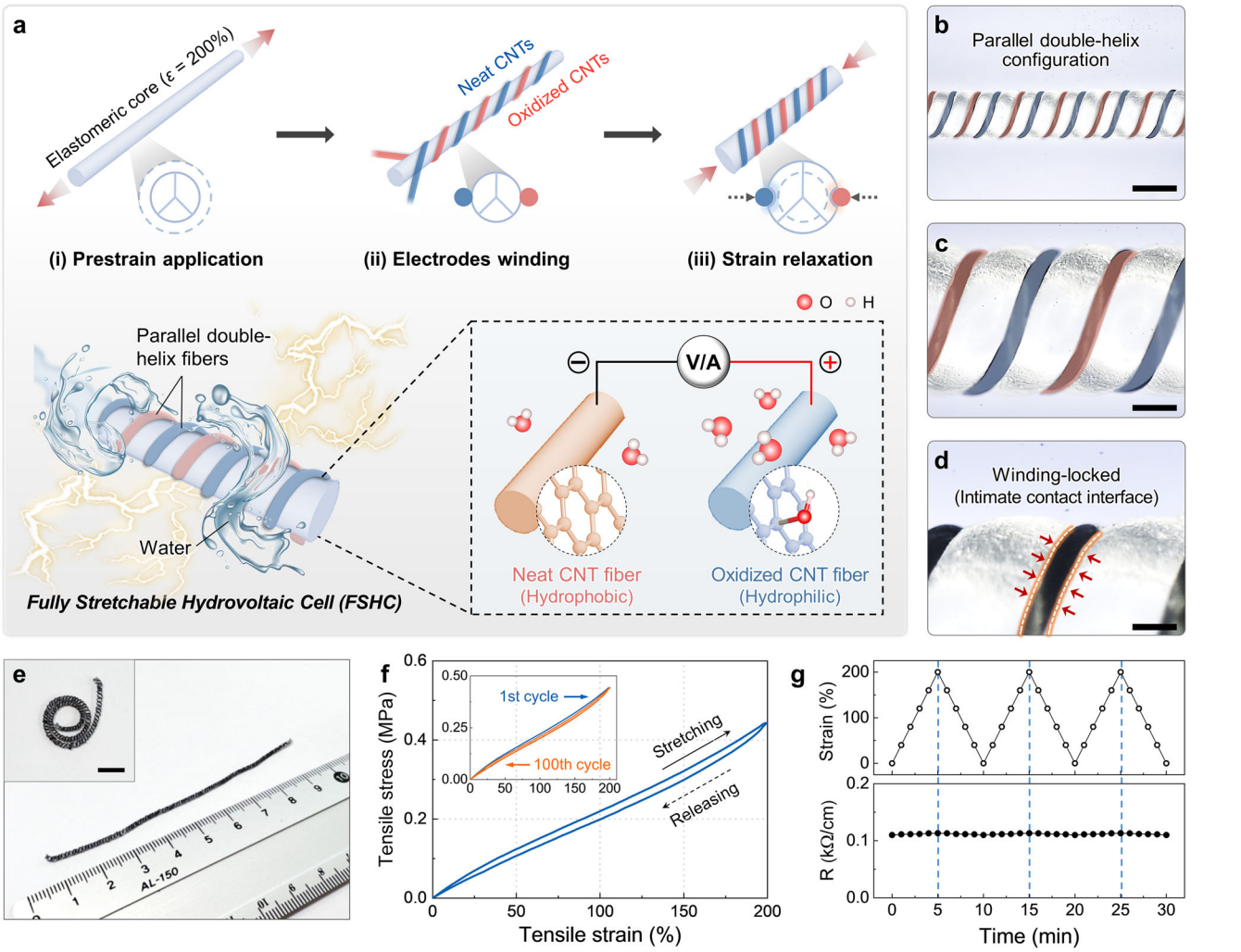

Fig. 1 | Design and structural characteristics of the fully stretchable hydrovoltaic cell (FSHC) based on carbon nanotube (CNT) fibers. a Schematic illustration of the FSHC fabrication process, comprising (i) prestraining of an elastomeric core (200% elongation), (ii) helical winding of neat CNT (NCNT) and oxidized CNT (OCNT) fiber electrodes around the prestrained core, and (iii) strain relaxation, where the elastomeric core returns to its original dimensions and induces self-locking of the CNT fibers onto the elastomeric core. When exposed to water, the FSHC generates electricity through hydrovoltaic effects, in which interactions between water molecules and the CNT fiber surfaces create a potential difference (inset). Water image from the Freepik website, which provides free stock photos licensed. Optical micrographs showing (**b**) the uniform parallel double-helix configuration of the FSHC (scale bar, 500 μm), **c** the constant interstitial spacing between the helical CNT fiber electrodes (scale bar, 150 μm), and **d** the intimate contact interface between the CNT fibers and the elastomeric core, formed by the winding-lock mechanism (scale bar, 100 μm). Here and elsewhere, red and blue shades are used to differentiate the individual CNT fiber electrodes. **e** Photograph of the completed FSHC demonstrating flexibility, with an inset showing the Fermat spiral configuration. **f** Cyclic loading–unloading curves under 200% strain, which demonstrate excellent elastic recovery, with an inset showing stress–strain curves before (black) and after (blue) the 100th cycle. **g** Time-dependent strain and resistance variations of the FSHC during cyclic stretching and releasing at 200% strain.

relaxation was observed in Fig. 1d, where the CNT electrodes appeared embedded in the elastomer surface. This observation confirmed the effectiveness of the winding-lock mechanism, in which the radial expansion of the elastomer during strain relaxation enhanced the interfacial adhesion. As a result, the CNT fibers were securely anchored to the core, thus improving the mechanical robustness of the FSHC under repeated deformations without slippage or delamination.

With its uniform and precisely organized parallel double-helix configuration, the as-fabricated FSHC (10 cm in length) exhibited good structural stability, maintaining a moderately straight profile in the free-standing state without the need for additional support (Fig. 1e). The inset further showed that the structure remains intact, without signs of entanglement or deformation, even in the Fermat spiral configuration. In addition, the FSHC exhibited excellent elastic recoverability under 200% strain (Fig. 1f). The cyclic loading–unloading curve (inset, Fig. 1f) demonstrated that the FSHC returned to its original state with negligible hysteresis even after 100 cycles. Furthermore, the time-dependent strain and resistance variations of the FSHC under cyclic stretching and releasing at 200% strain are shown in Fig. 1g. The resistance remained highly stable throughout the repeated deformation cycles, indicating excellent electromechanical durability. This stable resistance response under large mechanical deformation is a critical requirement for practical applications in stretchable and wearable electronics.

Electrical output performance of the nonstrained FSHC

Based on the above considerations, this section demonstrates the stable voltage output of the FSHC arising from asymmetric charge transfer at the CNT–water interface upon immersion. Specifically, when the OCNT (as the positive electrode) and NCNT (as the negative electrode) were connected to a digital source meter, the FSHC generated an open-circuit voltage of approximately 0.31 V that remained stable for 5000 s in water (Fig. 2a). Beyond this period, the output exhibited a slight decrease but still retained

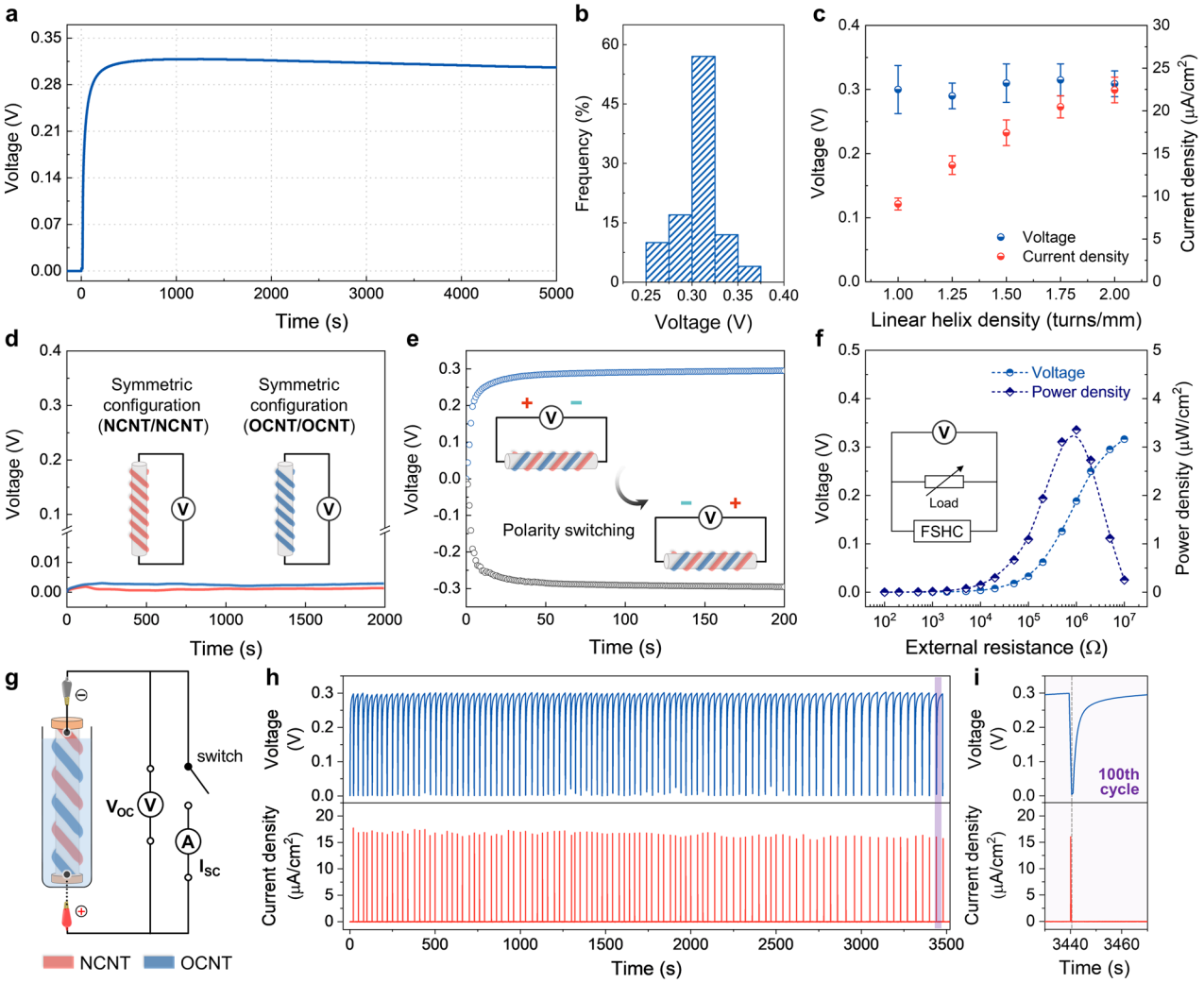

Fig. 2 | Electrical performance of the nonstrained FSHC in deionized water. **a** Voltage output of the FSHC, remaining stable at ~0.3 V. **b** Histogram of the voltage distribution. **c** Dependence of voltage and current density on linear helix density. **d** Negligible voltage generation of FSHCs with symmetric configurations (NCNT/NCNT or OCNT/OCNT). **e** Voltage response during polarity switching, with insets showing the circuit connection. **f** Generated voltage and power density as a function of external resistance (10^2 to 10^7 Ω), with an inset showing the equivalent test circuit diagram. **g** Schematic illustration of the charge–discharge test setup. **h** Cyclic performance during repeated discharge and autonomous recharge. **i** Enlarged view of the purple shaded region in (**h**), showing a typical discharge–charge cycle.

~87.7% of its peak value at 10,000 s (Supplementary Fig. 6). The voltage distribution showed a narrow window centered around 0.30 V (Fig. 2b), indicating the high reproducibility of the hydrovoltaic effect. Furthermore, a short-circuit current was detected when the cell was electrically connected in water (Supplementary Fig. 7).

To elucidate the underlying mechanism of this sustained voltage output, additional experiments were performed. First, rate-dependent galvanostatic discharging measurements were conducted to distinguish between capacitive and redox contributions. Supplementary Fig. 8a provides a schematic comparison of the voltage profiles of the two discharge behaviors. Capacitive-dominant behavior, arising from electric double layer (EDL) formation at the CNT–water interfaces, produces a linear voltage decay, whereas redox-dominant behavior, originating from electrochemical reactions at the two electrodes, yields a plateau-like profile. Actually, under relatively high current conditions (2.4–3.5 μA), the discharge curves exhibited a constant voltage slope characteristic of capacitive behavior (Supplementary Fig. 8b). This behavior can be described by $Q = C{\cdot}V$, where differentiation with respect to time gives $I = C{\cdot}dV/dt$. Above equation implies that the linear voltage decay at high discharge current stems from EDL formation and the pseudocapacitance of oxygen-containing groups at the electrode–water interfaces. In contrast, under lower current conditions (1.5–2.0 μA), a clear plateau was observed. Such behavior differs from capacitive discharge and indicates redox processes at the electrode–water interfaces. These findings explain the long-lived voltage plateau, demonstrating that redox reactions dominate the sustained voltage output, while EDL capacitance provides only a secondary contribution (Supplementary Fig. 8c). Moreover, the calculated redox charge ratio confirmed that redox behavior remained predominant even under high current conditions. We summarized and compared the current conditions, discharging curves, and electrochemical reaction associated with capacitive and redox behavior (Supplementary Table 1). Second, XPS analysis was performed to examine chemical composition changes in the CNT electrodes during the redox process. As shown in Supplementary Fig. 9a, b, both electrodes exhibited a pronounced increase in the oxygen peak (532 eV) after full discharge, raising the O/C atomic ratio from 0.11 to 0.22 for NCNT and from 0.27 to 0.34 for OCNT. High-resolution C1s and O1s spectra further revealed clear enhancements of the characteristic peaks at ~285.9 eV (C–OH) and ~532.9 eV (C–O) (Supplementary Fig. 9c, d). These results indicate that NCNT underwent oxidation while OCNT experienced reduction during discharge, strongly supporting that the sustained voltage under quiescent water originates from redox reactions at the CNT–water interfaces. In general, the electrical output of conventional hydrovoltaic systems decreases

once equilibrium is reached because they rely on ion-driven kinetic processes such as ion transport or diffusion. By contrast, the present FSHC maintained a stable voltage under quiescent water, suggesting that electrode-related electrochemical activity is the key to its persistent output. Even under partial immersion in deionized water (Supplementary Fig. 10), the generated voltage remained almost identical to that observed under full immersion; in this case, water evaporation has no observable effect on electricity generation. To further evaluate output stability, repeated wet–dry cycling tests were performed. As shown in Supplementary Fig. 11, the output voltage was stably reproduced over 300 successive cycles. The voltage profiles obtained during the final five cycles substantially overlapped with those from the initial five cycles (inset, Supplementary Fig. 11), implying that the wetting and drying process did not induce significant variability or transient perturbations in the voltage generation. The underlying mechanism was next examined by comparing voltage outputs in electrolyte solutions with different pH levels (Supplementary Fig. 12). The FSHC exhibited distinct voltage responses depending on the electrolyte composition. Specifically, the voltage was highest in 0.1 M HCl, followed by 0.1 M Na_2SO_4 and 0.1 M KOH, showing a strong dependence on proton concentration. This pH dependence can be explained by asymmetric redox reactions between NCNT and OCNT electrodes, as previously reported in the literature[31], as follows:

$$OCNT + H_2O + e^- \rightarrow (CNT - OH) + OH^- \quad (1)$$

while an oxidation occurs at the NCNT electrode as follows:

$$CNT + OH^- \rightarrow (CNT - OH) + e^- \quad (2)$$

These reactions directly involve OH^- ions, thereby making both the reaction kinetics and reduction potential strongly pH-dependent. In alkaline electrolytes, the high concentration of OH^- promotes the reverse reaction, leading to the lower reduction potential. In contrast, in acidic electrolytes, the high concentration of H^+ (corresponding to low concentration of OH^-) accelerates the forward reaction, resulting in a higher reduction potential. These results indicate that the availability of protons and their interactions with the CNT surface influence the hydrovoltaic performance.

In Fig. 2c, the cell's operation was evaluated by studying electricity generation as a function of the linear helix density and immersion speed. While the voltage output remained nearly unchanged, the short-circuit current increased with the increase with helix density, suggesting that the current was affected by the active surface area. This increase can be attributed to the extended CNT fiber length in higher-density configurations, which provided a larger effective contact area with water. The FSHC's performance was not influenced by changes in immersion speed (Supplementary Fig. 13), indicating that its operation differs from that of previously reported electrokinetic or fluidic devices. The dependence of voltage generation on asymmetric charge interactions was further verified in Fig. 2d. When symmetric electrode configurations with identical surface properties (*i.e.*, NCNT/NCNT or OCNT/OCNT) were used, the output voltage was negligible, demonstrating that differences in surface functionalization are critical for preserving charge separation and sustaining hydrovoltaic energy conversion. The role of electrode asymmetry was also confirmed by the polarity-switching tests (Fig. 2e). When the OCNT fiber was connected to the positive terminal, a positive voltage was observed (blue curve), whereas reversing the connections produced an inverted voltage (red curve), confirming the formation of a stable potential difference between the two electrodes. Collectively, these findings indicate that voltage generation is governed by asymmetric charge interactions at the CNT–water interface rather than by external ionic concentration gradients or electrokinetic effects.

The electrical power density of the FSHC is illustrated in Fig. 2f. The voltage increased with load resistance (100 Ω to 10 MΩ), reaching a peak power density of 3.35 μW/cm^2 at 1 MΩ. To evaluate the cycling stability, a charge–discharge test was then performed using an external circuit in which a switch was periodically toggled to control discharge and autonomous recharge (Fig. 2g). As shown in Fig. 2h, the FSHC exhibited a self-replenishing voltage after each discharge event and maintained stable charge–discharge behavior across multiple cycles, confirming its robustness under continuous operation. A closer look at an individual cycle (Fig. 2i) further underscored the reproducibility of the charge–discharge process, demonstrating that the FSHC can sustain long-term performance without significant degradation.

The effects of tensile deformation on the FSHC performance

Hydrovoltaic devices intended for use in stretchable and deformable electronics must maintain a stable electrical performance under mechanical strain. Unlike conventional fiber-based energy systems, which often suffer from electrical degradation due to mechanical failure, the double-helix configuration of the FSHC provides a unique structural advantage. By employing a winding-locked CNT fiber network, the FSHC can accommodate large tensile deformations while preserving its conductive pathways. However, despite the widespread adoption of helical structures in stretchable electronics, the precise structural changes that occur during elongation remain largely unexplored. Therefore, this section presents a detailed structural analysis of the FSHC under mechanical strain to demonstrate how its helical architecture adapts to stretching without compromising its electrical output.

First, the optical micrographs of the FSHC under increasing tensile strain (0–200%) are presented in Fig. 3a. As the strain increased, the helical CNT fibers gradually reoriented along the stretching direction while maintaining a uniform distribution. SEM images acquired after 200% strain showed no visible fiber fracture or delamination, confirming that the FSHC retained its structural integrity under large-strain deformation (Supplementary Fig. 14). This suggests that the double-helix structure underwent a systematic geometric transformation to accommodate strain without structural failure. These changes are quantitatively analyzed using an "unwound" model of a single helical turn (Fig. 3b). In this approach, each turn is conceptually unfolded into a straight segment, enabling a mathematical description of the effective fiber length under varying strain levels. This transformation is governed by three key geometric parameters: (i) the thickness (t) of the elastomeric core, (ii) the bias angle (θ) of the CNT windings, and (iii) the distance (d) between the NCNT and OCNT fiber electrodes. As shown in Supplementary Fig. 15, the variations in these parameters with increasing strain revealed a systematic structural adaptation. First, the elastomeric core thickness decreased due to Poisson's effect, which in turn influenced the winding geometry during uniaxial stretching. Second, the bias angle decreased, indicating progressive alignment of the CNT fibers along the stretching direction. Lastly, the inter-fiber spacing increased as the CNT fibers moved farther apart axially, thereby accommodating the applied strain while preserving the helical configuration. As a result, the calculated unwound fiber length remained nearly constant across all strain levels, with only minor deviations (Fig. 3c). This highlights how the double-helix structure efficiently distributed mechanical stress and prevented excessive elongation of individual CNT fibers. Consequently, the electrical resistance exhibited negligible variation, ensuring continuous electrical connectivity despite large deformations. These findings validate the strain-adaptive nature of the FSHC, demonstrating that the double-helix configuration preserved both mechanical resilience and electrical integrity under tensile strain.

Next, the influence of this strain-adaptive structure on the electrochemical performance of the FSHC was investigated. Because hydrovoltaic energy generation relies on interfacial charge interactions at the CNT–water interface, any mechanical deformation that compromises the conductive pathways or alters the electrode–electrolyte interactions could degrade the performance. Therefore, the intrinsic electrochemical properties of the individual CNT fiber electrodes were first characterized by cyclic voltammetry (CV) measurements in a three-electrode system with 0.1 M Na_2SO_4 electrolyte. As shown in Supplementary Fig. 16, the OCNT fiber exhibited a

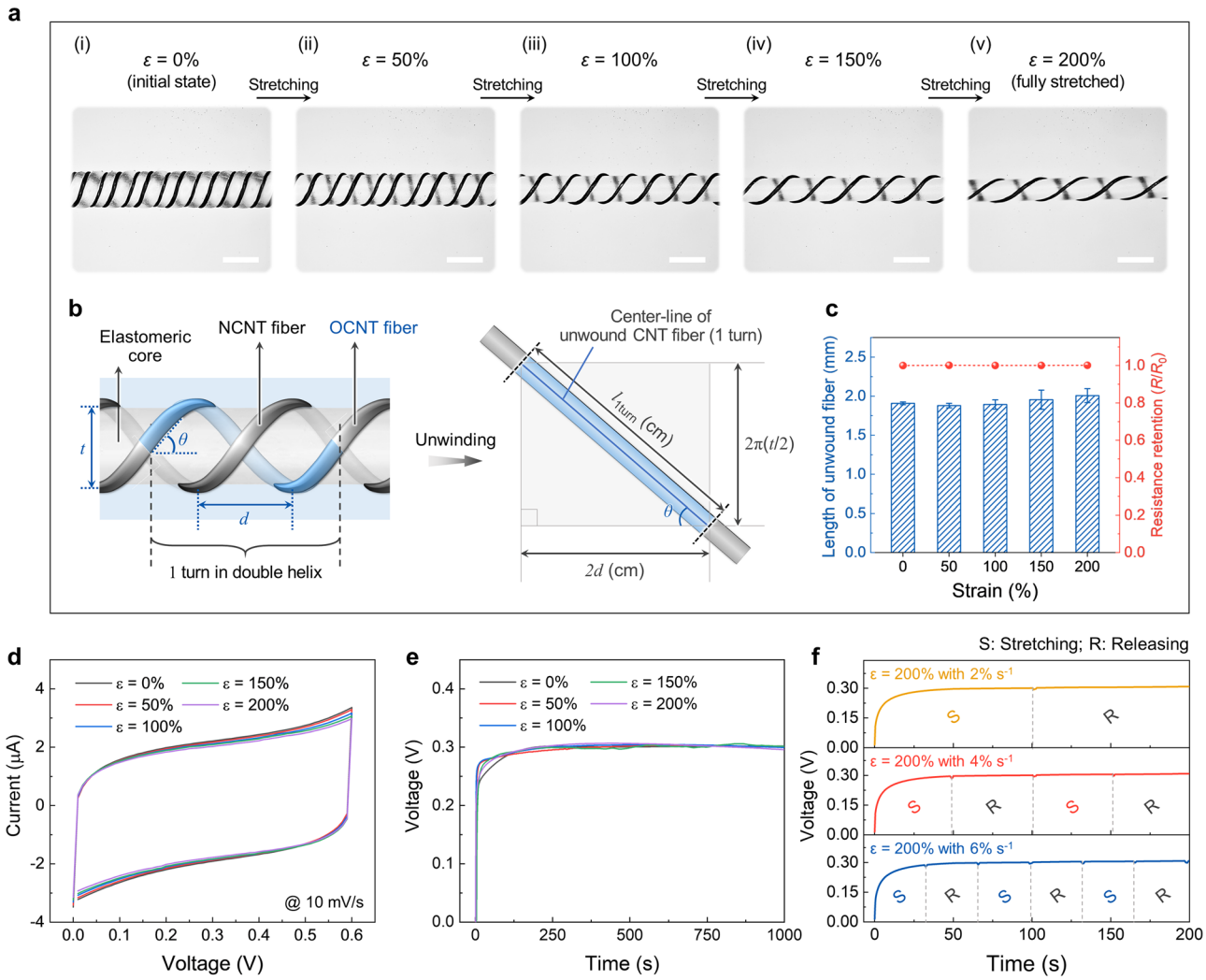

Fig. 3 | Stretching principle and electrical output of the FSHC under tensile strain. a Optical micrographs of the FSHC under applied strains of 0–200% (scale bar, 500 μm). **b** Schematic diagrams showing a single turn of the helical CNT fiber (left) and its unwound version (right), with the key structural parameters: core thickness (t), inter-fiber distance (d), and bias angle (θ). **c** Length of the unwound CNT fiber and resistance retention as a function of strain. **d** CV curves and **e** voltage outputs of the FSHC in the initial ($\varepsilon = 0\%$) and stretched states ($\varepsilon = 50$–200%). **f** Real-time voltage signals of the FSHC during stretching (S) and releasing (R) at strain rates of 2%/s (yellow), 4%/s (red), and 6%/s (blue).

226.1-fold larger CV area than that of the NCNT fiber, indicating markedly enhanced surface electrochemical activity due to the presence of oxygen-containing functional groups[38–41]. The electrochemical performance of the assembled FSHC was then demonstrated in its two-electrode configuration at scan rates ranging from 100 to 1000 mV/s (Supplementary Fig. 17). The observed rectangular CV curves without distinct Faradaic redox peaks were consistent with double-layer capacitance from CNTs and the pseudocapacitance from oxygen-containing groups. The effect of tensile strain on the electrochemical response of the FSHC was subsequently evaluated by CV measurements at 0%, 50%, 100%, and 200% strain (Fig. 3d). As shown in Supplementary Fig. 18, the corresponding capacitance remained nearly unchanged under all strain conditions, indicating that the FSHC maintained stable electrochemical behavior despite mechanical deformation. Preservation of the CV characteristics implies that the structural adaptability of the helical CNT network effectively prevented degradation of charge-transfer dynamics. The effect of strain on electrical output was also examined by measuring the voltage at different static elongations (Fig. 3e). The voltage remained stable at all strain levels, demonstrating that the double-helix structure accommodated deformation without disrupting the CNT–water interface. Moreover, the FSHC maintained stable performance over 500 stretching cycles at 200% strain (Supplementary Fig. 19 and inset). The voltage profiles at different stages during cycling were highly consistent. Finally, the durability of the FSHC under dynamic deformation was confirmed by cyclic stretching and releasing at strain rates of 2, 4, and 6%/s. As shown in Fig. 3f, the voltage output remained consistent regardless of the strain rate, indicating that hydrovoltaic performance was independent of stretching speed. No performance degradation was observed over repeated cycles, confirming both the mechanical resilience and electrical stability of the FSHC. Overall, these results demonstrate that the FSHC effectively maintains its structural and electrical integrity under both static and dynamic strains, making it a promising candidate for stretchable hydrovoltaic energy systems.

Fabric integration of the FSHC and its application in self-powered actuation

The feasibility of integrating the FSHC into a fabric-based system was investigated in this section. Given its fiber-based architecture, the FSHC could be incorporated into textiles without compromising the structural integrity, making it a promising candidate for applications requiring mechanical durability and electrical stability. A 10 cm-long FSHC was therefore sewn into a commercially available fabric glove (Fig. 4a). High-resolution images obtained before and after applying 50% tensile strain

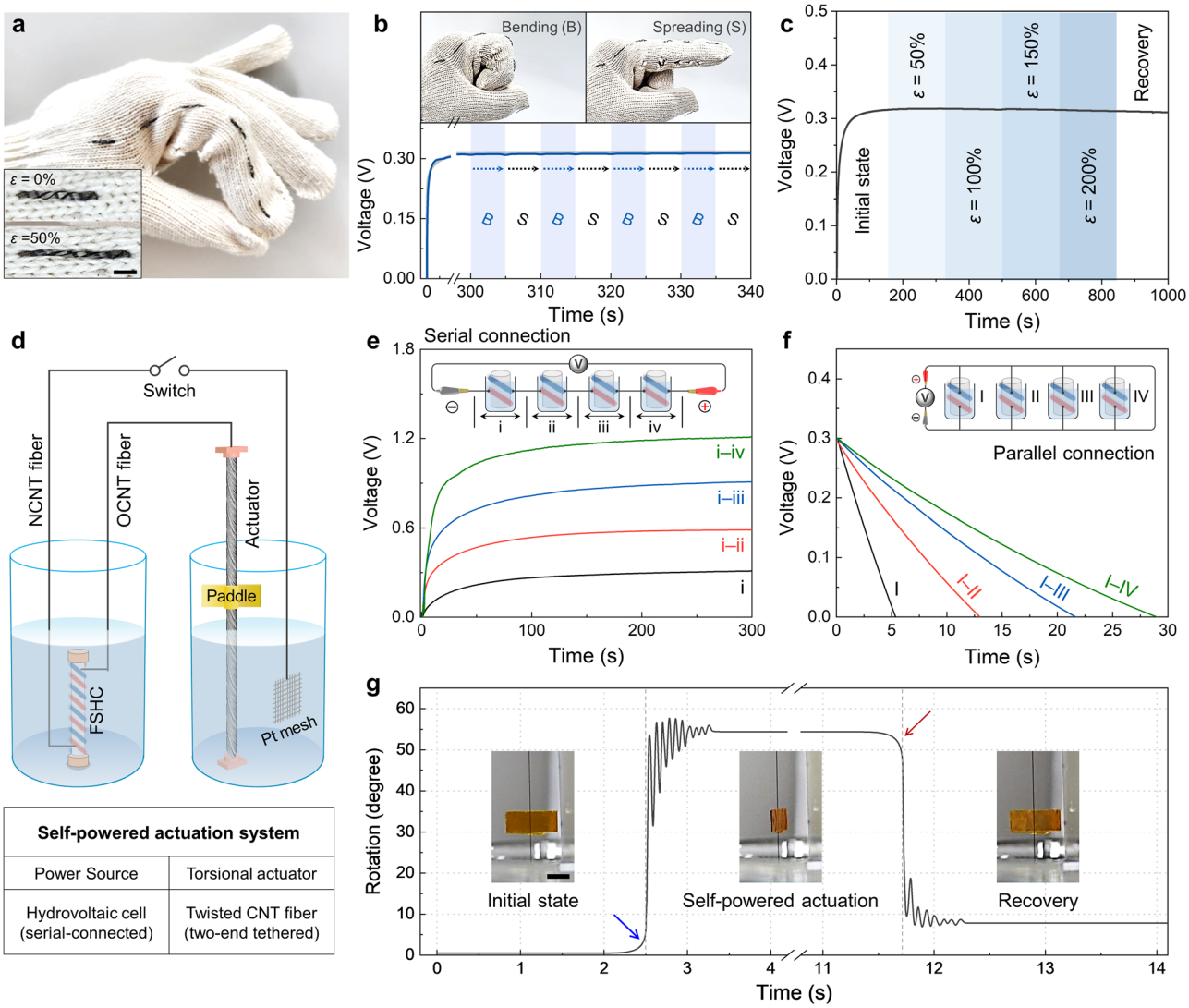

Self-powered actuation system	
Power Source	Torsional actuator
Hydrovoltaic cell (serial-connected)	Twisted CNT fiber (two-end tethered)

Fig. 4 | Integration of the FSHC into a fabric glove and its application in a self-powered actuation system. a Photograph of a 10 cm-long FSHC integrated into a commercial glove. Inset shows high-resolution images before and after applying 50% tensile strain (scale bar, 2 mm). **b** Real-time voltage response of the FSHC integrated into a fabric glove during repeated finger bending (B) and spreading (S) motions. **c** Voltage signals recorded under static strains of 0–200% followed by recovery, demonstrating electrical stability. **d** Schematic illustration of the self-powered actuation system, in which the FSHC supplies electrical energy to a twisted CNT fiber-based torsional actuator. **e** Voltage profiles of serially connected FSHCs (1–4 units, labeled i–iv). **f** Voltage profiles of parallelly connected FSHCs (1–4 units, labeled I–IV). **g** Paddle rotation angle of a two-end-tethered twisted CNT fiber driven by the FSHC, with inset photographs of the actuator in the initial state, during self-powered actuation, and after recovery.

(inset, Fig. 4a) confirmed that the FSHC maintained its structural integrity without any visible damage or delamination. To demonstrate the suitability of the FSHC for wearable applications, real-time voltage output of the integrated FSHC was monitored during repeated finger bending (B) and spreading (S) motions. As shown in Fig. 4b, the voltage signal (blue line) recorded during consecutive bending cycles remained highly stable, closely overlapping with the baseline signal (gray line) obtained prior to dynamic movement. These results confirm the feasibility of the FSHC for practical use in wearable scenarios. Electrical performance under mechanical strain was also evaluated by monitoring the voltage response during static stretching up to 200%. The results in Fig. 4c showed that the output voltage remained stable across all strain levels and was fully recovered upon relaxation, thereby confirming the mechanical resilience and ability of the FSHC to sustain hydrovoltaic energy generation under deformation.

In addition, the feasibility of utilizing the FSHC as a power source for a self-powered actuation system was explored. Given that the CNT fibers used in the FSHC are intrinsically twisted, they share structural similarities with twisted CNT actuators, which are known to exhibit untwisting behavior upon electrochemical volumetric expansion[42]. This property enables electrically driven torsional actuation when sufficient voltage is applied. Accordingly, a self-powered actuation system was designed in which the FSHC directly supplied energy to a twisted CNT fiber-based actuator (Fig. 4d). To provide adequate electrical input, the output voltage and capacity of the FSHC were adjusted by connecting multiple cells in series and parallel, respectively. The equivalent circuit diagrams are shown schematically in Fig. 4e, f (insets). The output voltage increased proportionally with the number of FSHCs connected in series, reaching 1.2 V with four units (Fig. 4e). In contrast, parallel connections effectively extended the discharging time, ensuring sufficient electrical stimulation for actuation (Fig. 4f). As shown in Fig. 4g, this approach successfully enabled self-powered torsional actuation of a twisted CNT fiber tethered at both ends. For this experiment, ten FSHCs were connected in series to generate an output voltage of ~3.11 V, which was sufficient to drive actuator (Supplementary Video 1). During actuation, the initial voltage of FSHCs gradually decreased to 0.09 V. The resulting voltage drop of 3.02 V (corresponding to the actual voltage applied to the actuator) can be attributed to the internal resistance of the self-powered system. In

addition, a transient peak current was observed at the moment of connection (Supplementary Fig. 20). This current response originates from the EDL charging at the CNT–electrolyte interface, where the applied potential drives ion migration in the electrolyte and their subsequent adsorption onto the CNT surface[42]. Such behavior is a typical feature of electrochemically driven actuators[43]. The fiber exhibited a rapid untwisting, leading to the rotation of an attached paddle. The actuation was fully reversible, with the fiber returning to its initial state after power removal.

The energy conversion efficiency of the self-powered actuation system was then quantified by comparing the electrical input from the FSHCs with the mechanical output of the torsional actuator. The electrical input energy was determined from the time-dependent voltage and current responses using following equation:

$$E_{in} = \int P\,dt = \int V(t) \cdot I(t)\,dt \tag{3}$$

where E_{in} is the electrical input energy and P is the instantaneous power. The calculated input energy was 1.04 μJ. The mechanical output energy was calculated from the paddle rotation and torque using following equation:

$$E_{out} = \int \tau(\theta)\,d\theta \tag{4}$$

where E_{out} is the mechanical output energy, τ is the torque, and θ is the paddle rotation, both obtained from frame-by-frame analysis of the recorded video. The paddle used for actuation had a mass of 1.8 mg and a moment of inertia of 4.8×10^{-12} kg·m², yielding an output energy of 9.2 nJ. Accordingly, the energy conversion efficiency of the self-powered actuation system was calculated to be ~0.88%. Although the efficiency was lower than that of existing electrochemical fiber or yarn actuators driven by external power (Supplementary Table 2), the primary aim of this study was to validate the practicality of the FSHC and to demonstrate the feasibility of a fully self-powered actuator system. The efficiency is expected to be further improved through future studies, including electrode structure optimization, device design refinement, and load matching. This proof-of-concept demonstration highlights the potential of FSHC as a scalable, sustainable energy source for autonomous, electrochemically driven actuation systems.

Discussion

Herein, we developed a FSHC with a parallel double-helix structure, wherein neat and oxidized CNT fibers (designated as NCNT and OCNT, respectively) were helically wound around an elastomeric core. The self-locking helical configuration of the CNT fibers provided mechanical robustness, allowing the FSHC to withstand large tensile deformations while maintaining its structural integrity. When immersed in water, the FSHC generated a stable open-circuit voltage and short-circuit current of ~0.31 V and 22.4 μA/cm², respectively, without requiring an ionic solution or flow of water. Supplementary Table 3 compares the driving force, environmental condition, and electrode condition of different hydrovoltaic mechanisms for clarifying the operating principle of the FSHC. Benefiting from its strain-adaptive design, the FSHC was able to withstand up to 200% tensile strain without any noticeable performance degradation. Its practical applicability was further demonstrated by integration into a fabric glove. In addition, connecting multiple FSHCs in series and parallel increased the power output sufficiently to drive a twisted CNT fiber-based torsional actuator. This proof-of-concept self-powered actuation system highlights the potential of the FSHC as a deformable energy harvester for electrochemically driven actuation. These findings establish the FSHC as a promising platform for stretchable hydrovoltaic energy harvesting, paving the way for integration into wearable electronics, autonomous actuation technologies, and next-generation self-powered devices.

Methods

Preparation of the CNT fiber electrodes

Five layers of CNT sheets (A-Tech system Co., Korea), each having a width of 20 mm and a length of 20 cm, were sequentially stacked. Each end of the CNT stack was then attached to adhesive carbon tape and rolled into a cylindrical structure. The resulting cylinder was mounted on the motor tip of a custom-built twisting machine, and a gradual twisting of 1000 turns per meter was introduced under a tensile load of 4 g. Oxidized CNT fibers were prepared by applying a potentiostatic voltage (5 V *vs.* Ag/AgCl for 30 s) in a 0.1 M Na_2SO_4 aqueous electrolyte, using a Pt mesh as the counter electrode and an Ag/AgCl electrode as the reference.

Preparation of the elastomeric core substrate

The elastomeric core was fabricated using commercially available dielectric silicone rubber (Ecoflex 0030, Smooth-On Inc., USA). The base and curing agent were mixed in a 1:1 ratio and degassed in a vacuum chamber for 30 min to remove any trapped air bubbles. The mixture was then injected into a 20-gauge syringe needle and cured in an oven at 80 °C for 100 min to form an elastomeric fiber.

Formation of the parallel double-helix structure with a self-locking effect

Opposite ends of the as-prepared elastomeric core were attached to opposite tips of a two-stepping motor, and a prestrain of 200% was applied to the core. The neat CNT (NCNT) fibers and oxidized CNT (OCNT) fibers were then helically wound around the stretched elastomeric core at a specific bias angle along its longitudinal axis. Upon release of the pre-applied strain, the elastic core contracted to form a winding-locked double-helix configuration, thus ensuring robust mechanical stability. Each CNT fiber electrode was electrically connected to a 200-μm diameter soft conductive thread (Soitex, Korea) using flexible silver/graphene paste (Graphene Supermarket, USA) to ensure stable electrical contact. To prevent unintended electrical leakage, all exposed silver/graphene paste regions were encapsulated in a thin layer of Ecoflex, thus providing both insulation and mechanical protection.

Characterization

Photographs and optical micrographs were captured using a digital camera (D750, Nikon, Japan) and an optical microscope (SMZ1270, Nikon, Japan), respectively. The microscopic surface morphology and structural characterizations were performed using a field-emission scanning electron microscope (FE-SEM, S-4600, Hitachi, Japan) operated at an accelerating voltage of 15–20 kV with a working distance of approximately 40 mm. The mechanical properties were evaluated using a universal testing machine (Instron 5966, Instron, USA) with a strain rate of 1 mm/min. The electrical resistance was measured using a digital multimeter (15 +, Fluke, USA). All the electrochemical experiments were performed using an electrochemical analyzer (Vertex EIS, Ivium, Netherlands). The chemical composition of the CNT fiber surface after electrochemical oxidation was analyzed using X-ray photoelectron spectroscopy (XPS, ESCALAB 250XI, Thermo Scientific, USA).

Electrical and electrochemical measurements

The generated open-circuit voltage and short-circuit current signals were recorded using a Keithley 2450 (Keithley Instruments, USA). All samples were short-circuited before testing to avoid any interference from static electricity. The electrochemical performance of the FSHC was evaluated using a two-electrode system, and the capacitance of a single electrode was calculated from the cyclic voltammetry (CV) curves using the equation $C = I/(dV/dt)$, where I and dV/dt denote the average discharge current and scan rate, respectively.

Construction of the self-powered actuation system

The self-powered actuation system was assembled in a two-electrode configuration, where the twisted CNT fiber actuator was used as the working electrode, a Pt mesh acted as the counter electrode, and 0.1 M Na_2SO_4 was

used as the electrolyte. Both ends of the fiber actuator were securely fixed to prevent unintended untwisting, thereby ensuring that only the lower half remained immersed in the electrolyte. A 1.8 mg paddle (35 times the weight of the CNT fiber) was attached at the midpoint of the fiber actuator as an optical marker, thereby facilitating clear visualization of torsional motion. The FSHC functioned as the direct power source, supplying electrical energy to drive charge injection-induced mechanical actuation. The paddle movement was recorded in slow motion at 480 frames per second using a high-speed camera (RX10 IV, SONY, Japan). Torsional actuation was quantitatively analyzed by tracking frame-by-frame variations in the projected paddle width, thus enabling precise measurement of the angular displacement as a function of time.

Data availability

The data that support the findings of this study are available from the corresponding author upon reasonable request.

Code availability

This study did not use custom code. No code is available.

Received: 7 May 2025; Accepted: 3 October 2025;
Published online: 18 November 2025

References

1. Visbeck, Z. Ocean science research is key for a sustainable future. *Nat. Commun.* **9**, 690 (2018).
2. Stephens, G. L. et al. An update on Earth's energy balance in light of the latest global observations. *Nat. Geosci.* **5**, 691–696 (2012).
3. Huang, Y., Cheng, H. & Qu, L. Emerging materials for water-enabled electricity generation. *ACS Mater. Lett.* **3**, 193–209 (2021).
4. Zhang, Z. et al. Emerging hydrovoltaic technology. *Nat. Nanotechnol.* **13**, 1109–1119 (2018).
5. Wang, K. & Li, J. Electricity generation from the interaction of liquid −solid interface: a review. *J. Mater. Chem. A* **9**, 8870–8895 (2021).
6. Yin, J., Zhou, J., Fang, S. & Guo, W. Hydrovoltaic energy on the way. *Joule* **4**, 1852 (2020).
7. Wang, X. et al. Hydrovoltaic technology: from mechanism to applications. *Chem. Soc. Rev.* **51**, 4902 (2022).
8. Yin, J. et al. Harvesting energy from water flow over graphene?. *Nano Lett.* **12**, 1736–1741 (2012).
9. Dhiman, P. et al. Harvesting energy from water flow over graphene. *Nano Lett.* **11**, 3123–3127 (2011).
10. Ghosh, S., Sood, A. K. & Kumar, N. Carbon nanotube flow sensors. *Science* **299**, 1042–1044 (2003).
11. Yin, J. et al. Waving potential in graphene. *Nat. Commun.* **5**, 3582 (2014).
12. Fei, W. et al. Waving potential at volt level by a pair of graphene sheets. *Nano Energy* **60**, 656–660 (2019).
13. Zhen, Z. et al. A wrinkled graphene and ionic liquid based electric generator for the sea energy harvesting. *2D Mater.* **6**, 045040 (2019).
14. Liu, R., Liu, C. & Fan, S. Hydrocapacitor for harvesting and storing energy from water movement. *ACS Appl. Mater. Interfaces* **10**, 35273–35280 (2018).
15. Yin, J. et al. Generating electricity by moving a droplet of ionic liquid along graphene. *Nat. Nanotechnol.* **9**, 378–383 (2014).
16. Wang, H. L. et al. High-efficiency single-droplet energy harvester for self-sustainable environmental intelligent networks. *Adv. Energy Mater.* **13**, 2302858 (2023).
17. Zheng, H. et al. Remote-controlled droplet chains-based electricity generators. *Adv. Energy Mater.* **13**, 2203825 (2023).
18. Yang, L. et al. An electrode-grounded droplet-based electricity generator (eg-deg) for liquid motion monitoring. *Adv. Funct. Mater.* **33**, 2302147 (2023).
19. Shao, W. et al. Field enhanced robust droplet electricity generation. *Adv. Funct. Mater.* **33**, 2302472 (2023).
20. Zhao, F. et al. Direct power generation from a graphene oxide film under moisture. *Adv. Mater.* **27**, 4351–4357 (2015).
21. Zhao, F. et al. Highly efficient moisture-enabled electricity generation from graphene oxide frameworks. *Energy Environ. Sci.* **9**, 912–916 (2016).
22. Zhen, Z. et al. A non-covalent cation-π interaction-based humidity-driven electric nanogenerator prepared with salt decorated wrinkled graphene. *Nano Energy* **62**, 189–196 (2019).
23. Yang, Y. et al. Moisture-electric–moisture-sensitive heterostructure triggered proton hopping for quality-enhancing moist-electric generator volume. *Nano-Micro Lett.* **16**, 56 (2024).
24. Kim, E. et al. Long-lasting moisture energy scavenging in dry ambient air empowered by a salt concentration-gradient cationic hydrogel. *Adv. Funct. Mater.* **35**, 2419710 (2025).
25. Xue, G. et al. Water-evaporation-induced electricity with nanostructured carbon materials. *Nat. Nanotechnol.* **12**, 317–321 (2017).
26. Li, L. et al. Sparking potential over 1200 V by a falling water droplet. *Sci. Adv.* **9**, eadi2993 (2023).
27. Yuan, R. et al. Hermetic hydrovoltaic cell sustained by internal water circulation. *Nat. Commun.* **15**, 9796 (2024).
28. Song, W. et al. Advances in stretchable organic photovoltaics: flexible transparent electrodes and deformable active layer design. *Adv. Mater.* **36**, 2311170 (2024).
29. Hao, Y. et al. Stretchable thermoelectrics: strategies, performances, and applications. *Adv. Funct. Mater.* **32**, 2109790 (2022).
30. Parida, K., Xiong, J., Zhou, X. & Lee, P. S. Progress on triboelectric nanogenerator with stretchability, self-healability and bio-compatibility. *Nano Energy* **59**, 237–257 (2019).
31. He, S. et al. Chemical-to-electricity carbon: water device. *Adv. Mater.* **30**, e1707635 (2018).
32. Zhang, M. et al. Strong, transparent, multifunctional, carbon nanotube sheets. *Science* **309**, 1215–1219 (2005).
33. Son, W. et al. Highly twisted supercoils for superelastic multi-functional fibres. *Nat. Commun.* **10**, 426 (2019).
34. Son, W. et al. Ply-hierarchical coiled yarns for two extreme applications: strain sensors and elastic supercapacitor electrodes. *Sens. Actuators B Chem.* **373**, 132775 (2022).
35. Son, W. et al. Double-helical carbon nanotube-wrapped elastomeric mandrel for electrical shortage-free, one-body multifunctional fiber systems. *Adv. Funct. Mater.* **34**, 2312033 (2024).
36. Beese, A. M. et al. Bio-inspired carbon nanotube-polymer composite yarns with hydrogen bond mediated lateral interactions. *ACS Nano* **7**, 3434–3446 (2013).
37. Shin, M. K. et al. Synergistic toughening of composite fibres by self-alignment of reduced garphene oxide and carbon nanotubes. *Nat. Commun.* **3**, 650 (2012).
38. Son, W. et al. Twist-stabilized, coiled carbon nanotube yarns with enhanced capacitance. *ACS Nano* **16**, 2661–2671 (2022).
39. Son, W. et al. Enhanced hydro-actuation and capacitance of electrochemically inner-bundle-activated carbon nanotube yarns. *ACS Appl. Mater. Interfaces* **15**, 13484–13494 (2023).
40. Lota, G. et al. Carbon materials modified by plasma treatment as electrodes for supercapacitors. *J. Power Sources* **195**, 7535–7539 (2010).
41. Banks, C. E., Davies, T. J., Wildgoose, G. G. & Compton, R. G. Electrocatalysis at graphite and carbon nanotube modified electrodes: edge-plane sites and tube ends are the reactive sites. *Chem. Commun.* **7**, 829–841 (2005).
42. Foroughi, J. et al. Torsional carbon nanotube artificial muscles. *Science* **334**, 494–497 (2011).
43. Ren, M. et al. Strong and robust electrochemical artificial muscles by ionic-liquid-in-nanofiber-sheathed carbon nanotube yarns. *Small* **17**, 2006181 (2021).

Acknowledgements
This work was supported by the National Research Foundation of Korea (NRF) grant funded by the Korea government (MSIT) (No. NRF-RS-2021-NR060086, No. RS-2023-00240008, and No. RS-2025-00560512), the Industrial Technology Innovation Program (Alchemist Project) (RS-2025-02634714) funded by the Ministry of Trade, Industry & Energy (MOTIE), Korea, and the Institute of Information & communications Technology Planning & Evaluation (IITP) grant funded by the Korea government (MSIT) (No. RS-2025-02263277).

Author contributions
W.S. was involved in the investigation and original draft writing. J.M.L. was involved in the investigation and methodology. H.S. and G.H.S. were involved in performing the experiments. S.B.C. and S.K. were involved in analyzing the experimental results. S.C. and S.J.K. were involved in the formal analysis. C.C. and S.H.K. were involved in conceptualization, review, and supervision. All authors read and approved the final manuscript.

Competing interests
The authors declare no competing interests.

Additional information
Supplementary information The online version contains supplementary material available at https://doi.org/10.1038/s41528-025-00493-6.

Correspondence and requests for materials should be addressed to Shi Hyeong Kim or Changsoon Choi.